

Prediction of Optimal Production Time during Underground CH₄ Storage with Cushion CO₂ Using Reservoir Simulations and Artificial Neural Networks

Johan Olav Helland,* Helmer André Friis, Mohsen Assadi, Łukasz Klimkowski, and Stanisław Nagy




Cite This: <https://doi.org/10.1021/acs.energyfuels.3c03382>



Read Online

ACCESS |

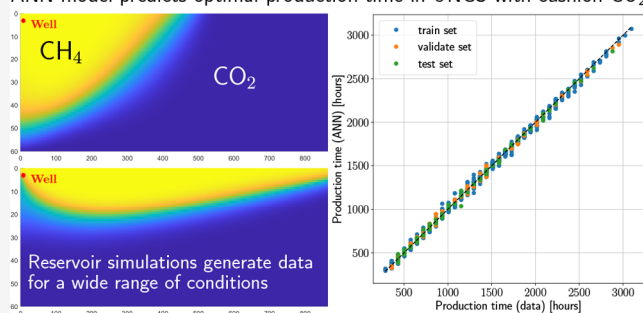
 Metrics & More

 Article Recommendations

 Supporting Information

ABSTRACT: Injection of carbon dioxide (CO₂) in aquifers for underground natural gas storage (UNGS) can improve the operating efficiency of the storage facility during gas injection and production and later serve as a solution for permanent CO₂ storage. However, mixing of the gases can lead to undesired CO₂ production during seasonal withdrawal periods, which requires costly treatment of the produced gas. This work quantifies the optimal production time (until the well stream exceeds 1% mole fraction of CO₂) in idealized, CO₂-filled reservoirs subjected to an injection and production cycle of methane (CH₄) in a single well. A set of 1200 compositional reservoir simulations with systematic variation of reservoir temperature, porosity, permeability, height, and injection time shows that reservoir height and permeability have the most significant impact on the production time. The generated data enable the development of artificial neural networks (ANN) that describe relations between the varied input parameters and the optimal production time with excellent accuracy. Reducing the amount of data sets in the ANN training from 1050 (87.5%) to 600 (50%) and augmenting the ANN output with other parameters, like maximal reservoir pressure, average CO₂ mole fraction, and well-block pressure at the end of production, only marginally reduces the accuracy of the data-driven models. In all cases, the developed ANNs exhibit an RMSE less than 0.02 and an R² score above 0.99. Hence, we conclude that trained and validated ANNs are useful tools to determine relations between important parameters in UNGS operations where CO₂ is used as cushion gas, with the aim at reaching higher CH₄ production time and larger amounts of delivered gas with minimal CO₂ production.

ANN model predicts optimal production time in UNGS with cushion CO₂:



1. INTRODUCTION

Subsurface storage technologies like carbon dioxide (CO₂) storage, underground hydrogen storage (UHS), and underground natural gas storage (UNGS) are technologies needed to mitigate climate change and to ensure a stable energy production in a transition from fossil fuels to renewable energy resources.¹ Natural gas (e.g., methane (CH₄)) is a cleaner fossil fuel than oil and coal that could play a role as an energy reserve to fluctuating wind and solar energy.² In UNGS, natural gas is injected and stored temporarily in salt caverns or subsurface reservoirs, such as depleted gas reservoirs or aquifers, before it is produced to meet fluctuations in demand due to seasonal variations (e.g., electrical heating in winter seasons) or variable energy supply from other sources.^{1,3}

Gas storage in an underground reservoir can benefit from using a cushion gas to improve the operating efficiency of the working gas by contributing with pressure support.^{3,4} The compressible property of CO₂, especially near its critical pressure, is an advantage for a cushion gas as it allows for large storage capacities of natural gas in the reservoir, while its expansion to lower pressure aids the gas production.⁵ Moreover,

the CO₂ will displace the formation water downward, and the injected natural gas will mainly contact the CO₂ in the overlying reservoir zone, which prevents extensive capillary trapping⁶ of the working gas during injection and production cycles. The injected CO₂ can be stored permanently in the reservoir after it has served as a cushion gas for UNGS. However, a potential drawback is that the mixing of gases in the reservoir can lead to undesired CO₂ production during continued seasons of injections and withdrawals.⁷

Important measures for a UNGS facility with cushion gas are^{3,4,8} (i) *total gas storage capacity*, which is the maximum volume of gas that can be stored in the reservoir; (ii) *cushion gas volume*, which is the amount of gas in the reservoir used to maintain pressure and withdrawal rates; (iii) *working gas*

Received: September 5, 2023

Revised: November 2, 2023

Accepted: November 6, 2023

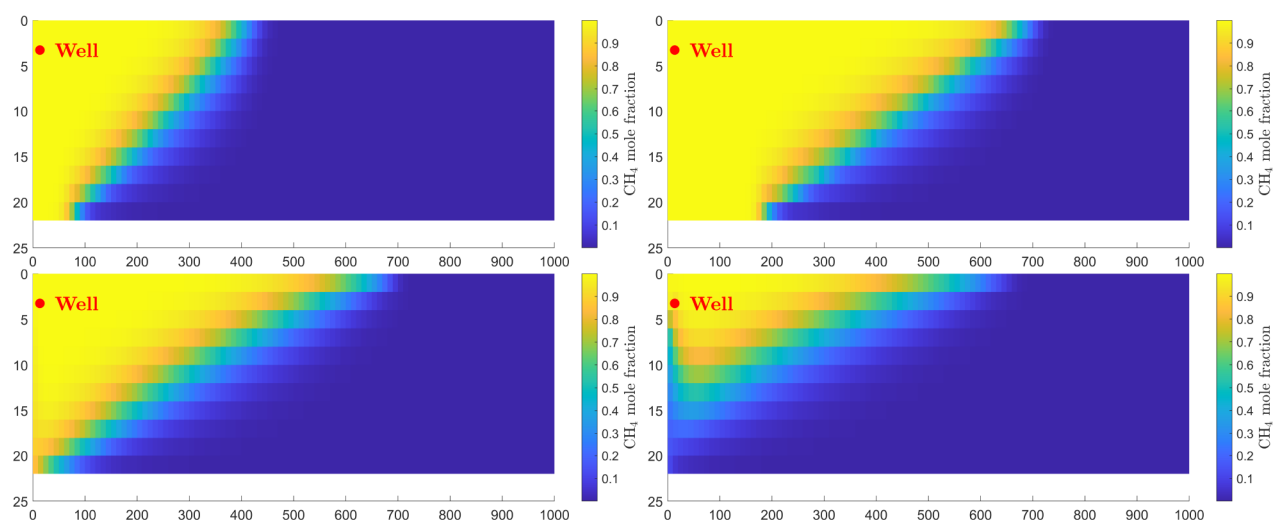


Figure 1. MRST simulation results of the CH₄ mole fraction distribution in the reservoir after 90 days (top, left), 180 days (top, right), 240 days (bottom, left), and 300 days (bottom, right). The simulation used grid blocks of size $10 \times 1 \times 2 \text{ m}^3$ and a maximal time step of 0.25 days.

capacity, defined as the total gas storage capacity minus the cushion gas volume; and (iv) *deliverability*, defined as the amount of gas that can be withdrawn from a storage facility per day. These storage measures depend further on parameters describing the reservoir and its conditions, including bulk volume and shape of the reservoir, porosity, permeability, reservoir pressure and temperature, and bottom-hole pressure in the wells. In practice, these measures are constrained by reservoir pressure that should stay below a critical maximum level to maintain mechanical stability of the reservoir,⁹ whereas the amount of cushion gas in the producing well stream should stay below given threshold values.

Reservoir simulation studies of UNGS with CO₂ cushion gas focus on demonstrating the advantageous density changes of CO₂ near its critical pressure in idealized reservoirs;⁵ the mechanical responses to pressure build-ups in idealized, yet inclined reservoirs;⁹ and simulations of working gas quality caused by mixing with cushion gas.^{7,10} Cao et al.⁷ simulated 15 years of UNGS operation where CO₂ and CH₄ were injected the first two years, followed by one-year cycles of CH₄ injection and production. Their results show that the extent of the CO₂/CH₄ mixing zone increases during production and decreases during injection. Further, both the mixing zone and the fraction of CO₂ in the produced gas increased with the CO₂ fraction used as a cushion gas. This presents limitations on the volume of the CO₂ cushion gas in a successful UNGS facility to ensure a low, acceptable CO₂ fraction in the produced gas.

The entry of data-driven methods has proven useful in research on CO₂ storage^{11–13} and on CO₂ injection for enhanced oil recovery,¹⁴ but there are to date few data-driven methodologies demonstrated for UNGS in depleted gas reservoirs or aquifers. In the literature, most data-driven approaches are concerned with describing the relations between gas deliverability, bottom hole pressure (BHP) in the well, and reservoir pressure.^{15,16} On the other hand, Mann and Ayala¹⁷ developed an artificial neural network (ANN) model aimed at determining the optimum design of a storage facility, but their model did not include information on which gas was considered as cushion gas, nor the reservoir conditions, both of which are important for the behavior of the gases and their mixtures.

When the cushion gas and working gas are different, it is important to predict the gas fractions in the produced well

stream over time to be able to implement measures that improve the deliverability of pure natural gas. This can be explored through the relationship between mole fractions in the well block versus production time, but such a relationship depends on the mixing behavior of the gases and will require accurate knowledge of the reservoir conditions (pressure and temperature). To date, data-driven methods based on ANN have not been developed to explore this relationship for UNGS operations in reservoirs with CH₄ as working gas and CO₂ as cushion gas. The main advantage with using ANN, once developed and validated, is that it typically takes only a fraction of a second to produce results that could take hours or days to produce with physics-based numerical simulation tools. Also, the strong interpolation capability of ANN suggests it is sufficient with results (obtained from simulations or measurements) for a finite number of discrete points in the parameter space for total coverage of the whole domain.

In this work, we perform systematic UNGS simulations in idealized reservoir geometries with one cycle of CH₄ injection and production using CO₂ as cushion gas, inspired by Oldenburg⁵ and Ma et al.⁹ The objective is to use the set of generated data to develop data-driven models based on artificial neural networks (ANN) that describe the maximal production time until the mole fraction of CO₂ in the well block rises above a certain level (set here as 1%). The ability to predict the duration of production in this manner is important, as higher CO₂ fractions in the well (with continued production) are less economically profitable due to costly treatment of the produced gas, and it may also be against legislation.⁷ The results can easily be translated to the total volume of gas delivered from the facility by the product of time and the constant production rate. In addition, we explore the accuracy of the ANN predictions when augmenting the output layer of the ANN with other important parameters, including well-block pressure (which is important to predict well performance in UNGS^{15,16}), maximal reservoir pressure, and average CO₂ mole fraction in the reservoir at the end of production. Following Ali,¹⁵ we also test how well these models perform when reducing the amount of data used in the training of the ANN. The paper is organized as follows: Section 2 describes the reservoir simulation tool, the conducted reservoir simulations, and the generated data, while section 3

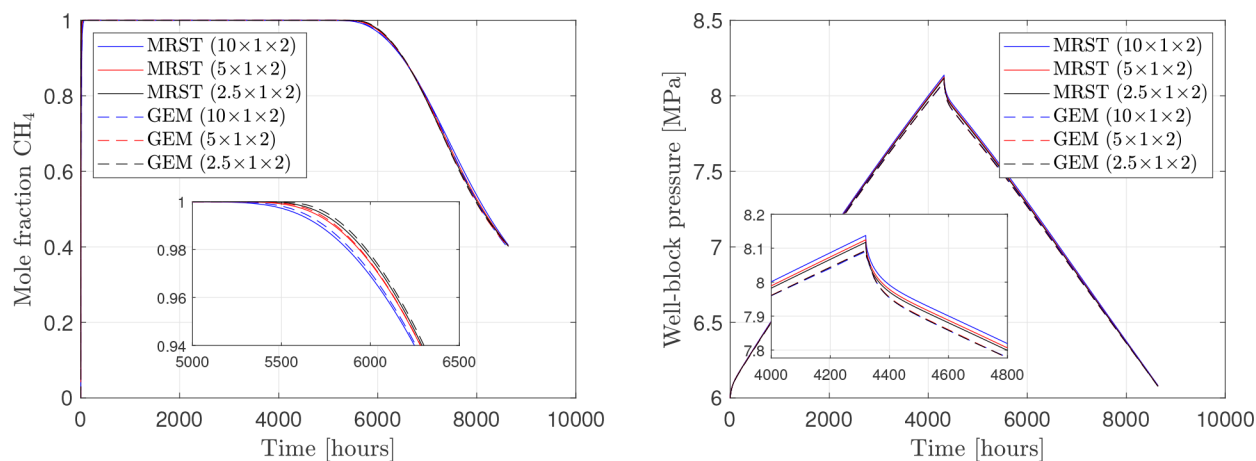


Figure 2. MRST and CMG-GEM simulation results for the CH₄ mole fraction (left) and pressure (right) in the well block over time using different grid-block sizes and a maximal time step of 0.25 days. The inset plots highlight the behavior in the initial stage of production.

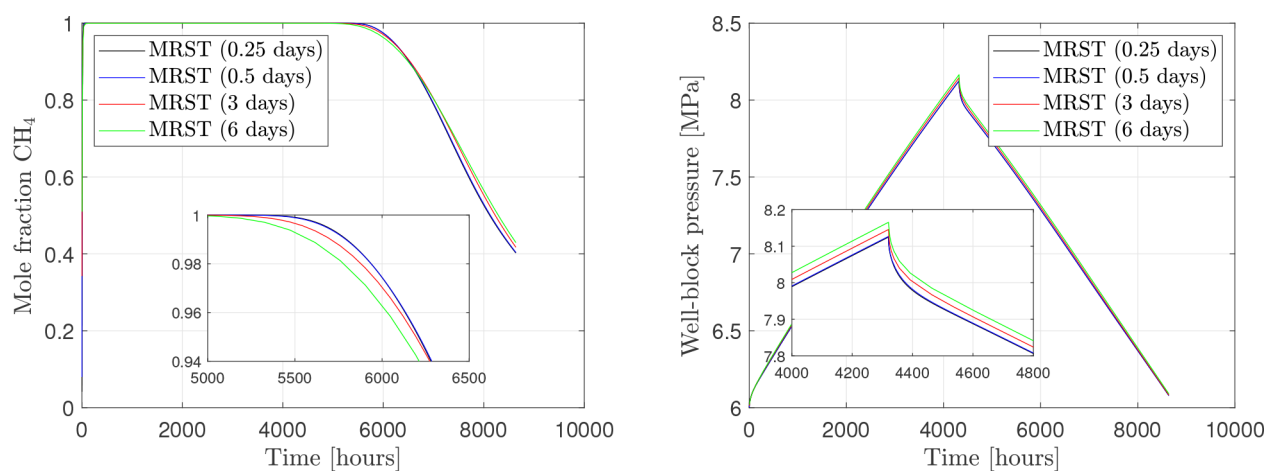


Figure 3. MRST simulation results for the CH₄ mole fraction (left) and pressure (right) in the well block over time using a grid-block size of 5 × 1 × 2 m³ and different maximal time steps.

describes the data-driven models and their performance. Section 4 provides conclusions and suggestions for future work.

2. RESERVOIR SIMULATION MODEL

This work uses the Matlab Reservoir Simulation Toolbox (MRST)^{18,19} to solve the mathematical model for two-

Table 1. List of Parameter Values Varied Independently in the MRST Simulations

temperature T [K]	reservoir thickness H [m]	porosity ϕ [frac.]	horizontal permeability K_h [mD]	injection time t_{inj} [days]
313.15	30	0.11	100	150
323.15	40	0.14	300	180
333.15	50	0.17	500	210
343.15	70	0.20	900	
	90		1300	

component flow of CO₂ and CH₄ in idealized reservoirs. MRST is an open-source software package for reservoir modeling and simulation written in Matlab and developed by SINTEF Digital in Norway, and the MRST module *Compositional* provides well-known solution strategies for compositional simulations.¹⁹ Lie and Møyner¹⁹ have previously benchmarked

the compositional module of MRST against the commercial reservoir simulator Eclipse 300²⁰ as well as AD-GPRS (the Stanford University research simulator).²¹ In section 2.2, we also present a comparison between MRST and the commercial reservoir simulator CMG-GEM.²²

2.1. Model Formulation. MRST uses a general formulation for two-component flow in a porous medium, where both components (in our case, CH₄ and CO₂) can exist in both liquid (l) and vapor (v) phases. We let x_1 and x_2 denote the molar fractions of the two components in the liquid phase, whereas y_1 and y_2 denote the corresponding molar fractions in the vapor phase, respectively. Moreover, the overall mole fraction of a component is denoted by z_i ($i = 1, 2$), and the liquid and vapor phase mole fractions read f_l and f_v . Clearly, the mole fractions must then fulfill the relations

$$x_l f_l + y_l f_v = z_i \quad (1)$$

where

$$f_l + f_v = 1 \quad (2)$$

We also need to introduce liquid and vapor phase saturations, s_l and s_v , such that

$$s_l + s_v = 1 \quad (3)$$

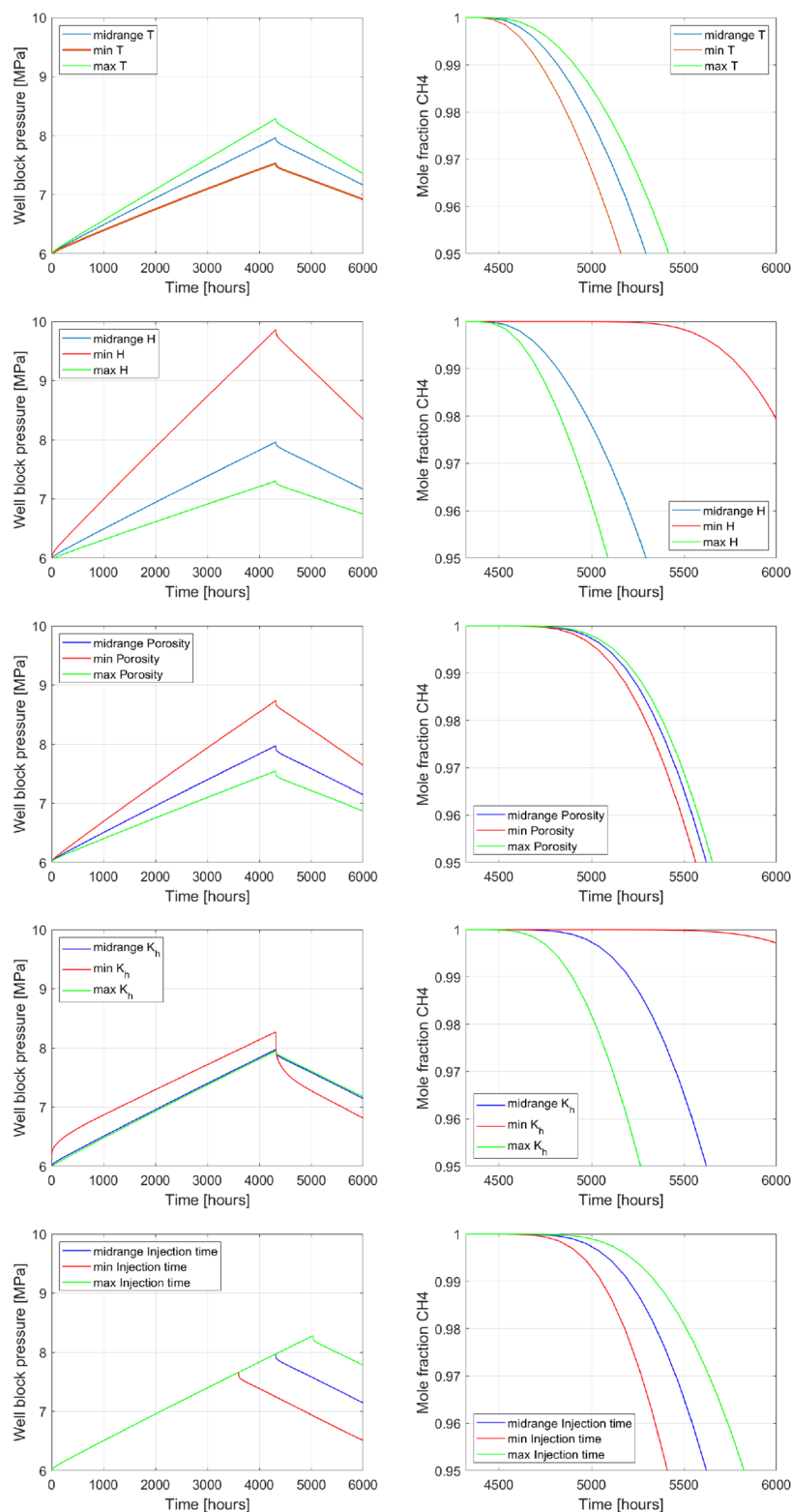


Figure 4. Well block pressure (left column) and CH₄ mole fraction (right column) from simulations with midrange parameter values compared to simulations with maximum and minimum values of each of the varied parameters: temperature T (first row), reservoir thickness H (second row), porosity ϕ (third row), horizontal permeability K_h (fourth row), and injection time t_{inj} (fifth row). In the case with varied t_{inj} , the CH₄ mole fraction is plotted against midrange time to enable comparison.

and mass fractions X_i and Y_i such that

$$X_i = \frac{\widehat{m}_i x_i}{\sum_{i=1}^2 \widehat{m}_i x_i} \quad (4)$$

and

$$Y_i = \frac{\widehat{m}_i y_i}{\sum_{i=1}^2 \widehat{m}_i y_i} \quad (5)$$

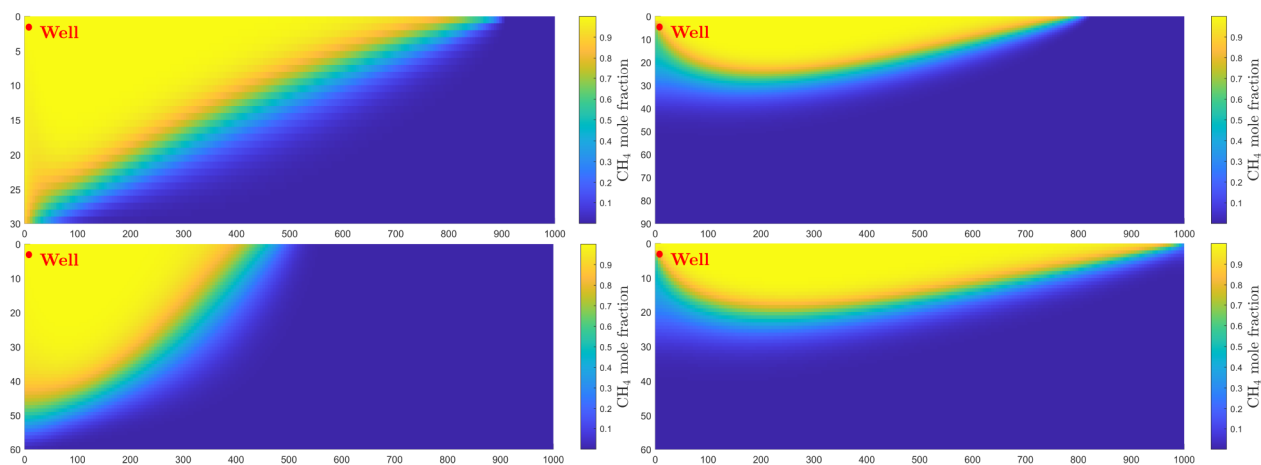


Figure 5. MRST simulation results of the CH₄ mole fraction distribution in the reservoir after 240 days for the simulations with midrange parameter values and variation of H (top) and K_h (bottom): (top, left) $H = 30$ m, (top, right) $H = 90$ m, (bottom, left) $K_h = 100$ mD, and (bottom, right) $K_h = 1300$ mD.

Table 2. Data Written to the File from MRST Simulations

parameters
height of reservoir H
temperature T
porosity ϕ
horizontal absolute permeability K_h
injection time t_{inj}
maximum reservoir pressure after injection, p_{max}
average reservoir CO ₂ mole fraction after injection, $\bar{z}_{CO_2}(t_{inj})$
average reservoir CO ₂ mole fraction after production, $\bar{z}_{CO_2}(t_{prod})$
average reservoir pressure after production, $\bar{p}(t_{prod})$
well-block pressure after production, $p_{wb}(t_{prod})$
production time until well block exceeds 1% CO ₂ mole fraction, t_{prod}

where \hat{m}_i denotes the molar mass of the component i .

The following mass continuity equation is then required for the mass of each component m_i ($i = 1, 2$):

$$\frac{\partial m_i}{\partial t} + \nabla \cdot \vec{U}_i = Q_i \quad (6)$$

where \vec{U}_i represents the appropriate total mass flux vector for each component, and Q_i is a source term for component i , which is closely connected to the actual well model being used. Moreover, the mass of each component and the corresponding total mass flux vector are defined as follows:

$$m_i = \phi(\rho_l s_l X_i + \rho_v s_v Y_i) \quad (7)$$

and

$$\vec{U}_i = -K \left(\frac{k_{rl}}{\mu_l} \vec{\Theta}_l + \frac{k_{rv}}{\mu_v} \vec{\Theta}_v \right) \quad (8)$$

Here, ϕ is the porosity and K is the absolute permeability of the porous medium; k_{rl} and k_{rv} are the liquid and vapor phase relative permeabilities; and ρ_l , μ_l , ρ_v , and μ_v are the density and viscosity of the liquid and vapor phases, respectively. Finally, the quantities $\vec{\Theta}_k$ (for $k = l, v$) reads

$$\vec{\Theta}_k = s_k \rho_k (\nabla p_k + \rho_k \vec{g}) \quad (9)$$

where \vec{g} is the acceleration of gravity.

The above set of equations are solved by an implicit numerical method, where equation-of-state methods based on thermodynamics determine the vapor and liquid compositions of the hydrocarbon system (i.e., flash calculations), as described in detail by Lie and Møyner.¹⁹ The model requires the equation of state (EoS) as a constitutive relationship, typically described by a third degree algebraic equation for the phase compressibility factor with coefficients depending on pressure, temperature, and mole fractions for a given mixture. The Peng–Robinson EoS²³ and Lohrenz–Bray–Clark viscosity correlation for hydrocarbon mixtures²⁴ are used as default settings in MRST and are also employed in the simulations presented in this work. Since we consider mixtures of CO₂ and CH₄ existing as vapor phase only ($s_l = 0$), the mole fractions reduce to $z_i = y_i$, $i = 1$ and 2 , and the flash calculations become trivial. Also, relative permeabilities are not required in this single-phase system; $k_{rl} = 0$ and $k_{rv} = 1$.

2.2. Comparison of Reservoir Simulators on a Test Case.

Before using the MRST simulator to generate data for data-driven methods, we perform simulations on a test case and compare the results against the commercial simulator CMG-GEM.²² The reservoir in the test case is a vertically aligned, rectangular 2D domain with a height of 22 m and a length of 1000 m. The thickness of the 2D geometry is 1 m. We consider an isotropic and homogeneous porous rock with absolute permeability $K = 1000$ mD and porosity $\phi = 0.3$. All boundaries are closed with imposed no-flow conditions. We place a vertical well with a radius of 10 cm in the upper left corner of the reservoir (3 m below the top boundary; see Figure 1). Initially, the reservoir is filled with CO₂, and we inject CH₄ at a constant rate for 180 days followed by production from the same well for another 180 days. Both the injection and production rates are set to 0.015 m³/s (given at standard surface conditions with a pressure of 1 atm and a temperature of 273.15 K). The initial reservoir pressure is 6 MPa, and the reservoir temperature is constant and equals $T = 313.15$ K. Hence, the reservoir pressure is above but the reservoir pressure is below the critical values for CO₂ ($T_{crit} = 304.13$ K and $p_{crit} = 7.38$ MPa). However, during CH₄ injection the reservoir pressure rises and the CO₂ transitions from the gas to a supercritical state. Thus, the simulations capture the sharp density changes with pressure in this region, which is advantageous for a cushion gas.^{5,9} When comparing the simulators on this test problem, we explore the impact of grid resolution through three sets of simulations with

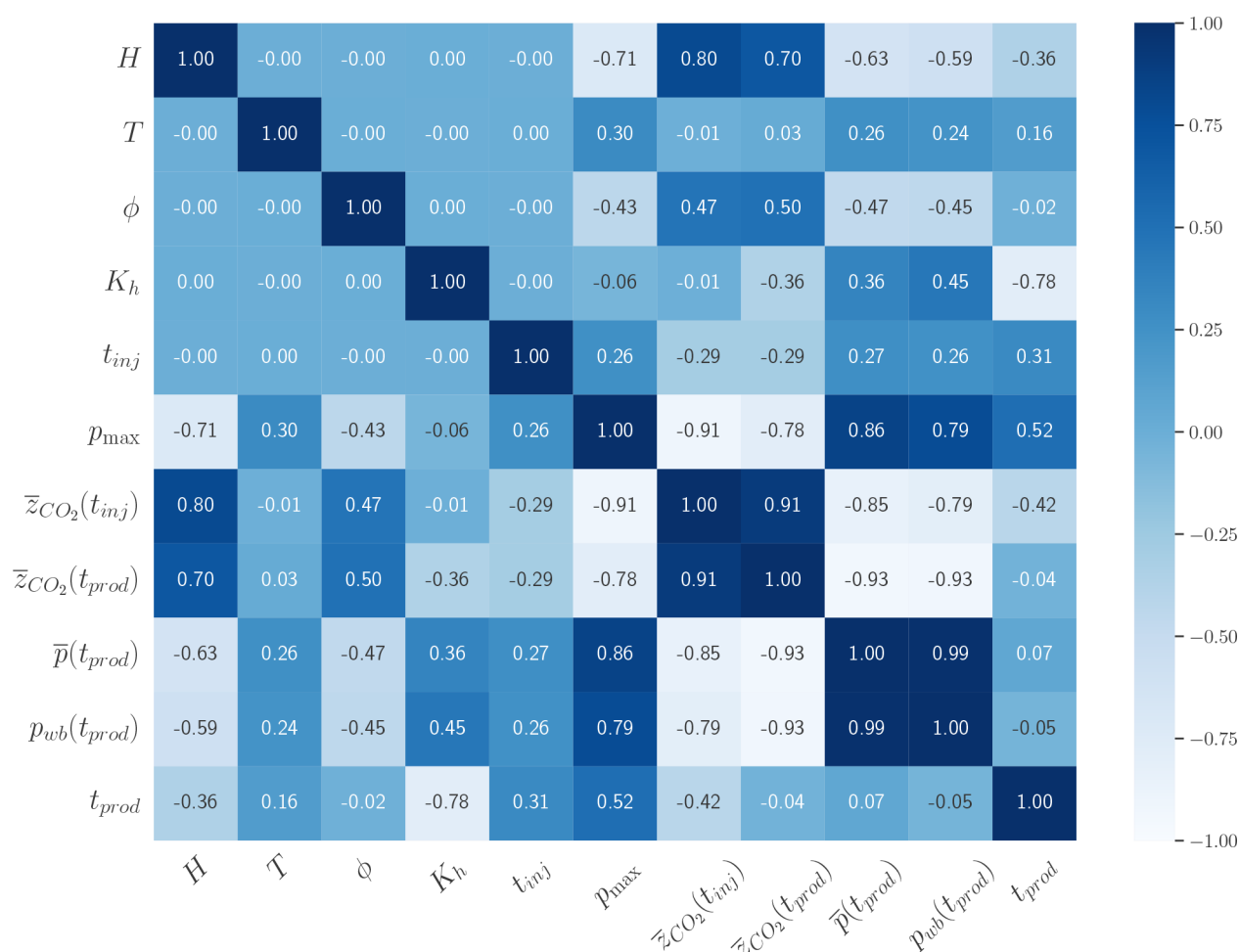


Figure 6. Pearson correlation matrix including all of the varied input parameters and the saved output from the 1200 MRST simulations.

grid-block sizes $10 \times 1 \times 2 \text{ m}^3$, $5 \times 1 \times 2 \text{ m}^3$, and $2.5 \times 1 \times 2 \text{ m}^3$, respectively. Due to differences in internal numerical implementations, the MRST and CMG-GEM simulators determine different, lower time steps adaptively during the simulations given a maximal time step as input. To minimize the differences in time steps between the simulators, a small maximal time step of 0.25 days was used for the comparison.

Figure 1 shows the CH_4 mole fraction field from the MRST simulation with grid-block size $10 \times 1 \times 2 \text{ m}^3$ after 90 days, 180 days (end of injection), 240 days, and 300 days. The lighter component, CH_4 , stays above the denser CO_2 with a mixing zone developing in between. We observe that the degree of CH_4/CO_2 mixing and the size of the mixing zone increases with time, particularly in the production phase, which is consistent with other works.⁷

Figure 2 compares the pressure and CH_4 mole fractions in the well block over time from the MRST and CMG-GEM simulations with different grid-block sizes. Generally, there is an excellent overall agreement between the two simulators. The well-block pressure increases throughout the injection period, and then it starts to decrease steeply right after the onset of production. At later stages the pressure still falls, but at a pace more similar to the increase in the injection period. Although the well-block pressure decreases slightly with increased grid resolution in the MRST simulations, it remains at a slightly higher level than in the CMG-GEM simulations where smaller grid blocks have negligible impact on the well-block pressure.

Obviously, the well-block CH_4 mole fraction equals one throughout the entire injection period and also throughout the early phase of the production period. A small discrepancy between the two simulators occurs for the well block CH_4 mole fraction during production, which starts to decline slightly earlier for the results produced by the MRST simulator and in simulations with coarser grids. However, both simulators successfully predict that the reduction of this mole fraction happens with a delay from the onset of production, and they both display convergence in the results with increased grid resolution. These minor differences in results are within acceptable tolerances and are likely caused by differences in the internal implementations of the numerical schemes in the two simulators. Slight differences in the numerical well models probably also contribute to some discrepancies in the end results.

For the MRST simulator, we also investigated the impact of using different maximal time steps in simulations with a grid-block size of $5 \times 1 \times 2 \text{ m}^3$. Finer temporal discretization leads to slightly lower well-block pressure and a slightly delayed decline of the CH_4 mole fraction in the well block during early stages of production, see Figure 3. As in the case of refined grids, the simulation results converge with a decreasing maximal time step.

2.3. Reservoir Simulations for Data-Driven Methods. With favorable results from the comparison of reservoir simulators, we proceed with using MRST to perform simulations with systematic variations of parameters in the idealized 2D case

with a single well to generate data for the data-driven methods. Such 2D setups promote investigations with the variation of a large number of independent parameters as the computational time for simulations in 2D being lower than in 3D. Hence, our objective is to explore the proof-of-concept in using data-driven methods to describe relationships between important parameters for UNGS with cushion CO₂ rather than describing storage in a real reservoir. These investigations still consider a reservoir with length $L = 1000$ m, initial pressure $p_0 = 6$ MPa, imposed no-flow conditions at the external boundaries, and the same well location at coordinate $(x, z) = (0, 3)$ (with a downward positive z -axis). The rate for CH₄ injection and production is 0.015 m³/s (at standard conditions). However, now we consider anisotropic and homogeneous media, in which the vertical permeability K_v (perpendicular to bedding) and horizontal permeability K_h (parallel with bedding) are different and related as $K_v = 0.1K_h$. Typically, a permeability anisotropy ratio $K_v/K_h < 1$ occurs due to grain sorting and bedding laminations, while $K_v/K_h > 1$ occurs in rocks with fractures perpendicular to the bedding.²⁵ Even for sandstones without fractures, this ratio could vary significantly.²⁶ However, using a permeability ratio $K_v/K_h = 0.1$ for non-fractured rock is considered as a rule-of-thumb in the absence of available data.²⁵

The simulations aim at describing the behavior in the top zone of reservoirs where we assume only CH₄ and CO₂ are present. As this zone is above the gas/water transition zone, the water saturation is small and irreducible and can be neglected for practical purposes. Measurements on sandstone core samples show that the irreducible water saturation can be very small, ranging from 0.02 to 0.13 in Bentheimer sandstone.²⁷ Thus, in our simulations, we interpret the reservoir height H as the height of the top zone in the reservoir that contains only CH₄ and CO₂. We note that the absence of a water saturation is also consistent with similar simulation studies.⁹

The parameters that are varied independently in the simulations are the reservoir temperature T , vertical reservoir height H , porosity ϕ , horizontal permeability K_h , and injection time t_{inj} . This also leads to variation in the volumes of the cushion gas (CO₂) and working gas (CH₄). For this set of simulations, we use higher spatial grid resolution and slightly lower time step resolution as a trade-off between accuracy and computational efficiency. Grid-block size is always set to $5 \times 1 \times 1$ m³, which means that the number of grid blocks used in a simulation depends on reservoir height H . Further, the maximal time step size is set to 3 days. Convergence tests have shown that this is an adequate resolution for these problems (cf. section 2.2).

Table 1 shows the range and resolution of the parameters that we vary independently in the simulations. Note that the chosen ranges in porosity and permeability are typical for sandstone,²⁸ while the temperature range captures various reservoir conditions encountered in sedimentary basins.²⁹ Thus, we have carried out a total number of 1200 ($= 4 \times 5 \times 4 \times 5 \times 3$) simulations with different parameter combinations. The midrange of each parameter is $T = 328.15$ K, $H = 60$ m, $\phi = 0.155$, $K_h = 700$ mD, and $t_{inj} = 180$ days. A simulation with midrange parameter values was then compared with new simulations in which the midrange value of one parameter at a time was substituted with its maximum and minimum value. These simulations show that the vertical reservoir height H and horizontal permeability K_h have the most significant impact on the CH₄ mole fraction in the well block during production among the varied parameters, especially for parameter values in

the interval between the minimum and midrange values (see Figure 4). Thus, this interval employs a finer resolution in the selection of values of these parameters than that in the interval between the midrange and maximum values, as shown in Table 1. Figure 4 shows that the CH₄ production is most favorable for low H and K_h . This is further investigated in Figure 5, which shows the CH₄ mole fraction distribution in the reservoir after 60 days of production. When H is large, CH₄ occupies the upper part with CO₂ located entirely below, separated by a mixing zone. For small H , CH₄ reached the bottom boundary during injection, which causes CH₄ to occupy the upper left diagonal area during the simulation. The impact of horizontal permeability K_h is quite similar; a large K_h leads to considerable lateral transport of CH₄ during injection and production, while a low K_h yields a CH₄ distribution that enters a larger fraction of the vertical distance. We also observe that the CH₄/CO₂ mixing zone is larger with increasing H and decreasing K_h , consistent with other studies.⁷

While the simulations shown in Figures 4 and 5 were performed with equal time periods for injection and production, the data saved for the data-driven methods consider the state in which the well-block CO₂ mole fraction exceeds 1% as the end of production. The production time when this occurs is denoted as t_{prod} . Table 2 lists all of the data written to file from the 1200 simulations, where the first five parameters are the varied input parameters, and the last six are output parameters. Hence, from the end of injection, we save the maximum reservoir pressure p_{max} and the average mole fraction of CO₂ in the reservoir, $\bar{z}_{CO_2}(t_{inj})$, while from the end of production, we again save the average CO₂ mole fraction in the reservoir, $\bar{z}_{CO_2}(t_{prod})$, as well as the average reservoir pressure $\bar{p}(t_{prod})$, the well-block pressure $p_{wb}(t_{prod})$, and the production time t_{prod} . These data were saved in an .xlsx file where the parameters are organized in different columns with one row of data per simulation (see Supporting Information).

To explore correlations among the set of 11 parameters, we calculated the Pearson correlation matrix, as shown in Figure 6. The Pearson correlation coefficient takes values within the interval $[-1, 1]$, and it describes the degree of linear correlation between two parameters. Coefficients with values -1 or 1 indicate perfect linear correlation, while values far within these limits (close to zero) indicate either no correlation or other nonlinear correlations. Obviously, as the five input parameters were varied independently they show no correlation. Among the output parameters, the maximum pressure p_{max} exhibits high correlation with the parameters that alters the pore volume, such as H and ϕ , while it has a lower degree of correlation with K_h , as is also evident from Figure 4. Production time shows the least correlation with ϕ among the input parameters, consistent with Figure 4. We also note that $\bar{p}(t_{prod})$ and $p_{wb}(t_{prod})$ show similar behaviors, which indicates that the reservoir pressure only has a marginal spatial variation in a simulation although it varies significantly over time. The average CO₂ mole fractions after injection and production, $\bar{z}_{CO_2}(t_{inj})$ and $\bar{z}_{CO_2}(t_{prod})$, also show relatively similar behaviors, except that $\bar{z}_{CO_2}(t_{prod})$ shows higher correlation with K_h .

3. DATA-DRIVEN MODELING FOR UNGS WITH CUSHION CO₂

For the data-driven modeling, we explore feed-forward neural networks with backpropagation, utilizing the data generated

Table 3. Overview of the Input and Output Parameters for the ANN Models Generated in This Study

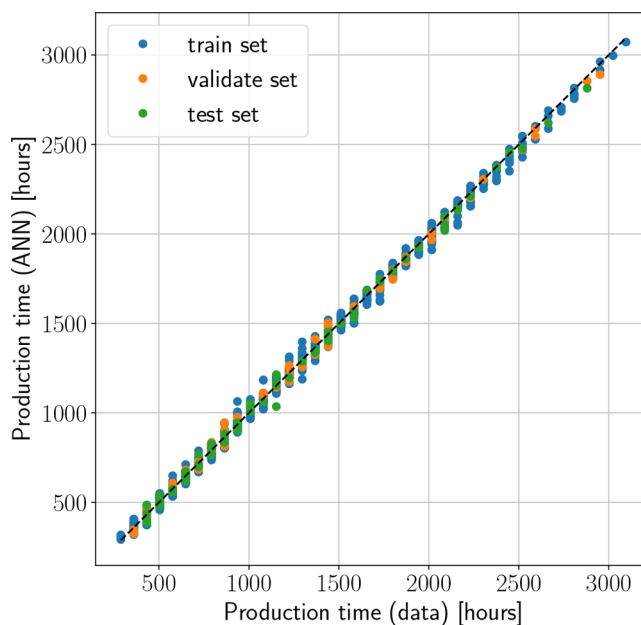
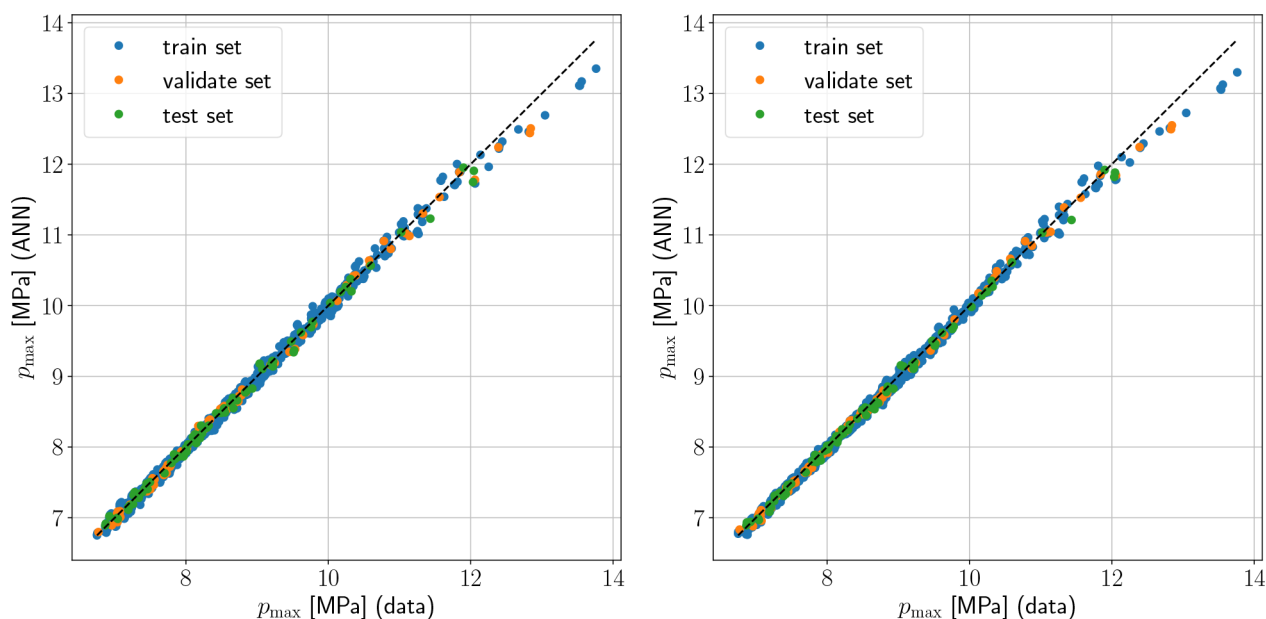
ANN model	input parameters (#)	output parameters (#)
case 1	$H, T, \phi, K_{hr}, t_{inj}$ (5)	p_{max} (1)
case 2	$H, T, \phi, K_{hr}, t_{inj}, V_{CO_2}$ (6)	p_{max} (1)
case 3	$H, T, \phi, K_{hr}, t_{inj}$ (5)	t_{prod} (1)
case 4	$H, T, \phi, K_{hr}, t_{inj}, V_{CO_2}$ (6)	t_{prod} (1)
case 5	$H, T, \phi, K_{hr}, t_{inj}, V_{CO_2}, p_{max}$ (7)	t_{prod} (1)
case 6	$H, T, \phi, K_{hr}, t_{inj}$ (5)	t_{prod}, p_{max} (2)
case 7	$H, T, \phi, K_{hr}, t_{inj}$ (5)	t_{prod}, p_{wb} (2)
case 8	$H, T, \phi, K_{hr}, t_{inj}$ (5)	t_{prod}, \bar{z}_{CO_2} (2)
case 9	$H, T, \phi, K_{hr}, t_{inj}$ (5)	$t_{prod}, p_{max}, p_{wb}$ (3)
case 10	$H, T, \phi, K_{hr}, t_{inj}$ (5)	$t_{prod}, p_{max}, p_{wb}, \bar{z}_{CO_2}$ (4)

from the MRST simulations. The ANN models were implemented in a *Python* environment using *TensorFlow* and the high-level *Keras* library. This code framework offers high flexibility in determining the optimal structure of the ANN and in training the models. These tools have also been utilized in data-driven methods that describe trapping mechanisms in CO_2 storage.¹¹

Before developing the ANN models, the data from the MRST simulations were rescaled to the interval $[0, 1]$, which is crucial to achieving numerical stability in the training, as the data vary significantly in magnitude. Then the data rows from the 1200 simulations were shuffled randomly, with the possibility to replicate the shuffle if needed. In the shuffled data, we extract the N_v first set of rows as the validation data set, the N_v next set of rows as the test data set, and the large remainder of the data as the training data set. Here, the training data set is used only for training of the ANN, and the test data set is used only to explore the predictive capability of the trained model. In this work, the role of the validation data is merely to evaluate the performance during the training to determine when to terminate the training based on accuracy and to avoid overfitting. Hence, the validation data set does not directly cause modification of parameters (weights and biases) in the neural network.

Table 4. RMSE and R^2 for ANNs with a Single Output and Different Number of Inputs, Using 1050 Data for Training and 75 Data Each for Validation and Testing

ANN model	training (87.5%)		validation (6.25%)		testing (6.25%)	
	RMSE	R^2	RMSE	R^2	RMSE	R^2
case 1	0.0106	0.9962	0.0130	0.9965	0.0104	0.9965
case 2	0.0105	0.9963	0.0114	0.9973	0.0097	0.9970
case 3	0.0105	0.9975	0.0118	0.9975	0.0110	0.9975
case 4	0.0108	0.9975	0.0127	0.9970	0.0113	0.9973
case 5	0.0110	0.9973	0.0115	0.9976	0.0122	0.9969

**Figure 8.** Calculation of t_{prod} versus corresponding data sets from training, validation, and testing, using the ANN model for case 3.**Figure 7.** Calculation of p_{max} versus corresponding data sets from training, validation, and testing, using ANN models for case 1 (left) and case 2 (right).

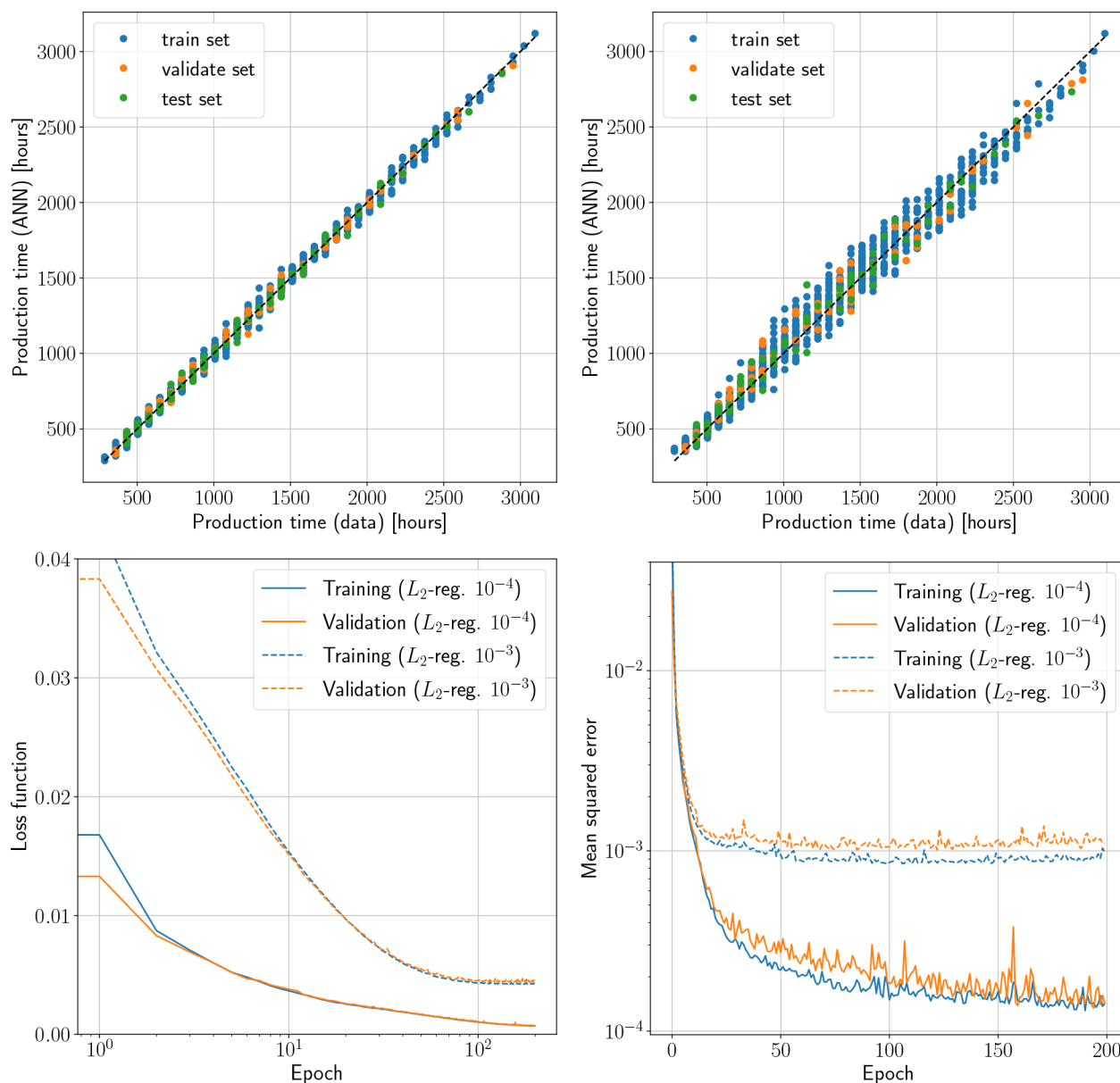


Figure 9. (Top) Calculation of t_{prod} versus corresponding data sets from training, validation, and testing, using the ANN model for case 5 with L_2 regularization weights 10^{-4} (top, left) and 10^{-3} (top, right). (Bottom) Loss function and mean squared error vs epoch for training and validation data sets during training of the ANN model for case 5.

Table 5. RMSE and R^2 for ANNs with Multiple Outputs, Using 1050 Data for Training and 75 Data Each for Validation and Testing

ANN model	training (87.5%)		validation (6.25%)		testing (6.25%)	
	RMSE	R^2	RMSE	R^2	RMSE	R^2
case 6	0.0159	0.9932	0.0173	0.9942	0.0163	0.9933
case 7	0.0134	0.9940	0.0162	0.9936	0.0133	0.9948
case 8	0.0129	0.9958	0.0136	0.9963	0.0116	0.9968
case 9	0.0149	0.9932	0.0169	0.9936	0.0152	0.9932
case 10	0.0163	0.9916	0.0186	0.9920	0.0161	0.9922

When developing the optimal choice of the ANN structure, we started with a small number of hidden layers and a small number of neurons in each layer. Then, the networks were trained by systematically increasing the number of neurons and layers until no significant improvement in the results was

Table 6. RMSE and R^2 for ANNs with Multiple Outputs, Using 900 Data for Training and 150 Data Each for Validation and Testing

ANN model	training (75%)		validation (12.5%)		testing (12.5%)	
	RMSE	R^2	RMSE	R^2	RMSE	R^2
case 6	0.0152	0.9935	0.0162	0.9942	0.0155	0.9940
case 7	0.0128	0.9949	0.0141	0.9945	0.0127	0.9948
case 8	0.0151	0.9942	0.0145	0.9955	0.0149	0.9945
case 9	0.0145	0.9936	0.0144	0.9946	0.0146	0.9932
case 10	0.0180	0.9893	0.0185	0.9908	0.0171	0.9904

observed. For each network the choice of activation function and specifications of the learning rate were altered. We also investigated the possibility of deactivating a fraction of neurons in each layer (called “dropout fraction”) and the use of regularization weights in every layer based on a metric (for

Table 7. RMSE and R^2 for ANNs with multiple outputs, using 600 data for training, and 300 data each for validation and testing

ANN model	training (50%)		validation (25%)		testing (25%)	
	RMSE	R^2	RMSE	R^2	RMSE	R^2
case 6	0.0148	0.9942	0.0163	0.9940	0.0172	0.9916
case 7	0.0139	0.9937	0.0157	0.9925	0.0162	0.9914
case 8	0.0142	0.9951	0.0158	0.9945	0.0162	0.9930
case 9	0.0145	0.9934	0.0157	0.9928	0.0162	0.9915
case 10	0.0171	0.9906	0.0183	0.9903	0.0189	0.9885

example, L_2 -norm) that will add a penalty to the total loss function. These functionalities are useful means to avoid overfitting in ANN models. As the optimization method, we use the Adam optimizer,³⁰ which is a stochastic gradient descent

method, while mean squared error (MSE) was used both as the loss function and as the metric to assess the performance of the training of every epoch. The training of the ANN was terminated when the MSE versus epoch curve reached a flattening trend with an MSE value around 10^{-4} for both the training data set and the validation data set. We observed this behavior after 200 epochs and terminated the training then.

Based on this experimentation, ANN models with two hidden layers and a relatively large number of neurons were developed. The optimized models use the rectified linear unit (ReLU) function as the activation function. The training also made use of a slightly declining learning rate and L_2 -regularization weights in each layer set to 10^{-4} . Although we explored the use of nonzero dropout fractions of neurons in the development, this feature did not improve the results.

In this work, we optimize the neural network structure in two ANN models that predict p_{\max} and t_{prod} separately. Then, we use

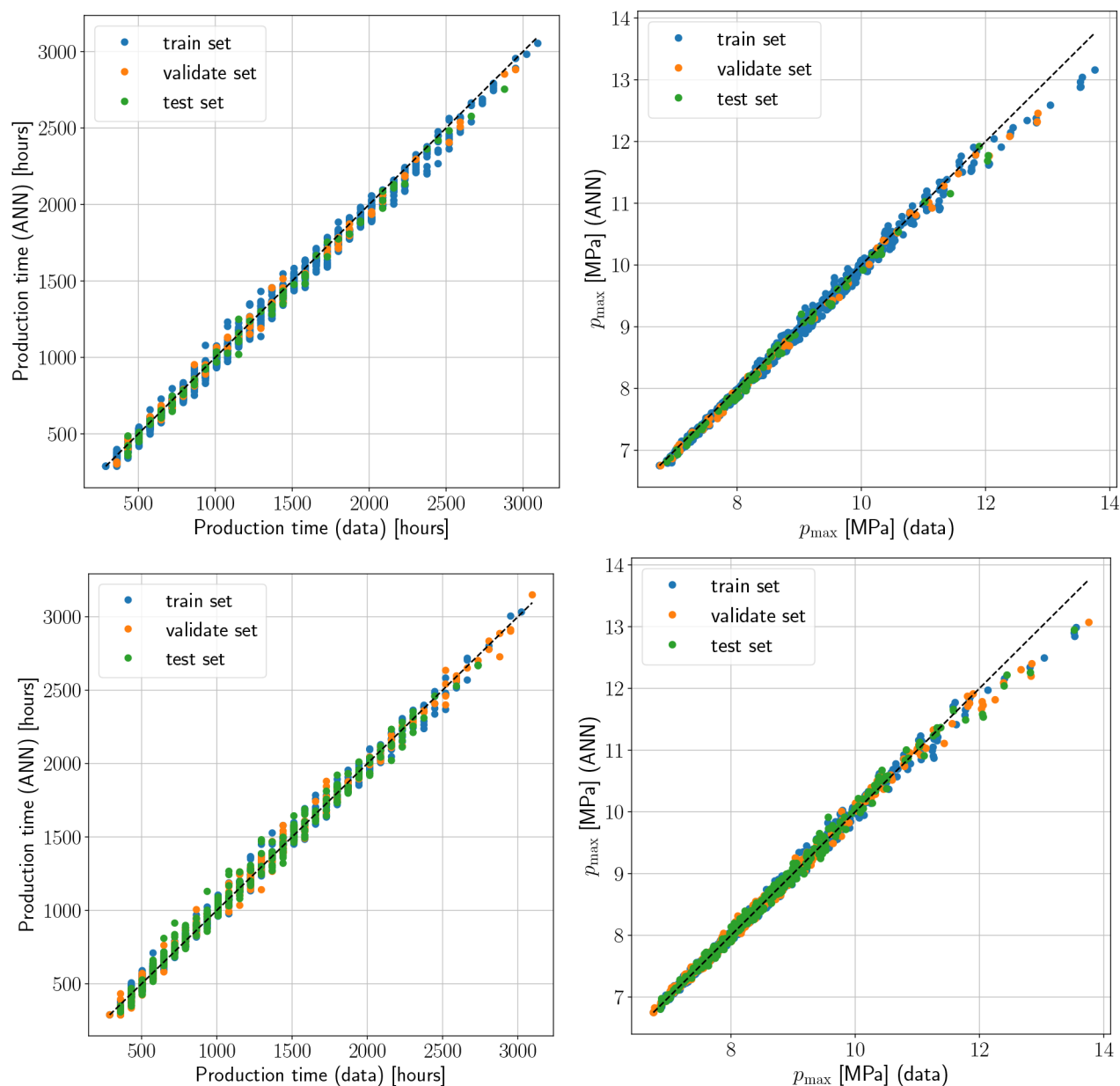


Figure 10. Performance of ANN models for case 6 with respect to the output parameters t_{prod} (left) and p_{\max} (right), using 87.5% of the data in the training and 6.25% for validation and testing (top) and 50% of the data in the training and 25% for validation and testing (bottom).

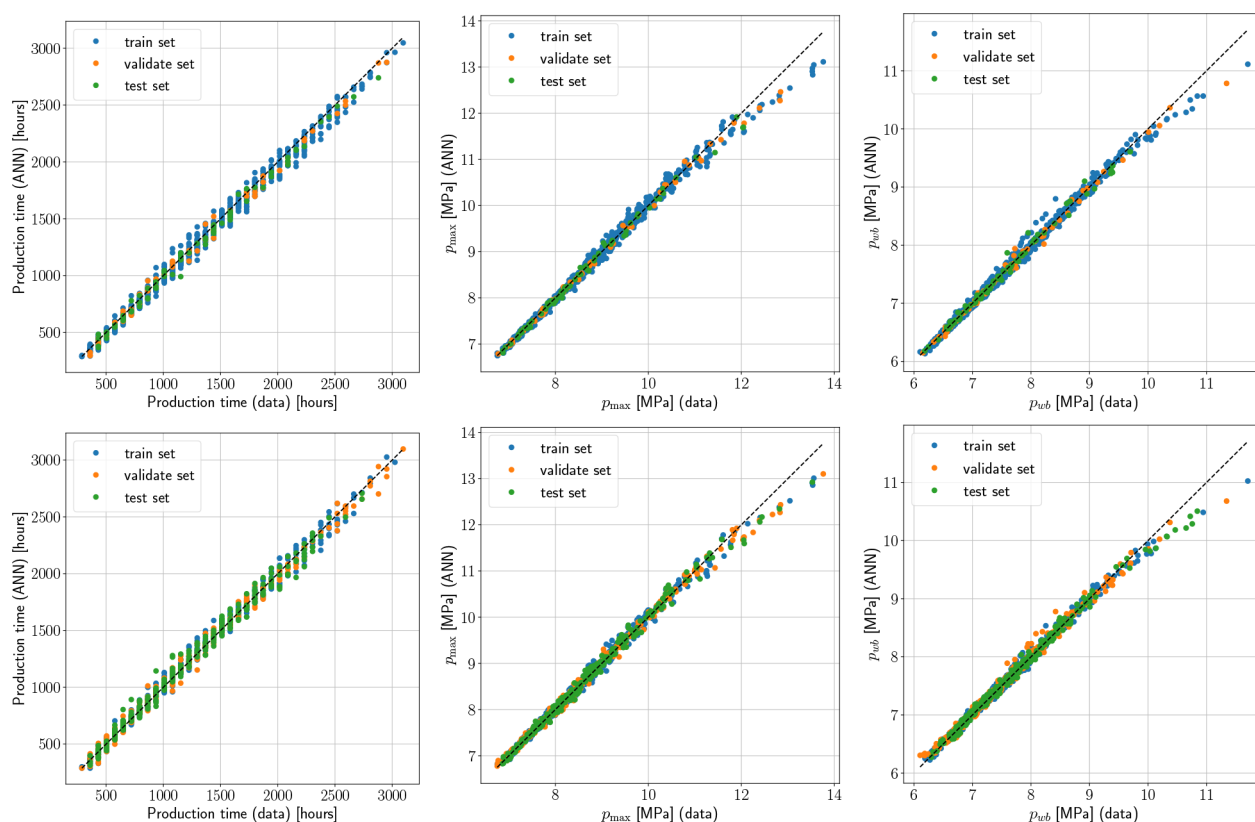


Figure 11. Performance of ANN models for case 9 with respect to the output parameters t_{prod} (left), p_{max} (middle), and p_{wb} (right), using 87.5% of the data in the training and 6.25% each for validation and testing (top) and 50% of the data in the training and 25% each for validation and testing (bottom).

these network architectures in further experimentation to explore if the training of these models with the addition of derived input parameters and other output parameters impacts their predictive capabilities. Table 3 provides a summary of the input and output of these ANN models, organized from case 1 to case 10.

3.1. ANN Models with One Output Parameter: Maximum Pressure and Production Time. We begin by developing ANN models with a single output parameter (cases 1 to 5 in Table 3), for both the maximal pressure p_{max} and the production time t_{prod} . The size of the validation set and that of the test set were both set as $N_v = 75$ (6.25% each), leaving data from 1050 (87.5%) simulations for the training, which is consistent with data shares used in training of models for CO_2 storage.¹² The optimized ANN model for p_{max} has 12 and six neurons in the first and second hidden layer, respectively. In case 1, the input layer consists of the five parameters varied independently in the simulations (H , T , ϕ , K_{lv} , t_{inj}). The inclusion of input parameters derived from other input parameters has been shown to improve previously developed ANN models.¹⁷ Case 2 explores this aspect by including the volume of CO_2 cushion gas, V_{CO_2} , as a derived input parameter to the input layer of this network before the training was repeated. Since only CO_2 is present in the reservoir initially, V_{CO_2} is obtained from the formula for original gas in place:²³

$$V_{\text{CO}_2} = \frac{V_{\text{B}}\phi}{B_{\text{g}}}, B_{\text{g}} = \frac{p_{\text{stc}} T}{T_{\text{stc}} p} Z(p, T) \quad (10)$$

Here, V_{B} is bulk reservoir volume, B_{g} is the gas volume formation factor, which can be readily calculated from the initial condition based on reservoir pressure p_0 , temperature T , and compressibility factor Z , as well as the pressure and temperature at standard conditions, p_{stc} and T_{stc} respectively.

Figure 7 shows that both the ANN models for case 1 and case 2 exhibit excellent performance with respect to the training, validation, and test data sets, and they perform very alike. The most conspicuous discrepancy between the ANN predictions and the data occurs at a high p_{max} where the amount of data is scarce. Using the data on the nondimensional form (rescaled to the interval $[0, 1]$), we calculated the root mean squared error (RMSE) and R^2 score to compare the ANN performance, as shown in Table 4. The addition of V_{CO_2} as the derived input parameter in case 2 results in only marginal improvement of the ANN compared with case 1.

The optimal network structure in the ANN model for t_{prod} consists of 42 neurons in the first hidden layer and 15 neurons in the second hidden layer. Here, case 3 takes the five parameters varied in the simulations as input (H , T , ϕ , K_{lv} , t_{inj}), while case 4 augments this input with the cushion CO_2 volume V_{CO_2} . Case 5 extends the input to both V_{CO_2} and p_{max} . The RMSE and R^2 score in Table 4 do not reveal a clear trend in improved performance by the addition of input parameters (case 4 and case 5). Cases 3 to 5 all perform excellently with an RMSE below 0.013 and an R^2 score above 0.997, of which case 3 obtains the best results on most of the estimates. Figures 8 and 9 confirm this very alike behavior for case 3 and case 5, with respect to the training, validation, and test data sets. Figure 9 also explores the impact of using 10^{-3} rather than 10^{-4} as regularization weights in the L_2 -

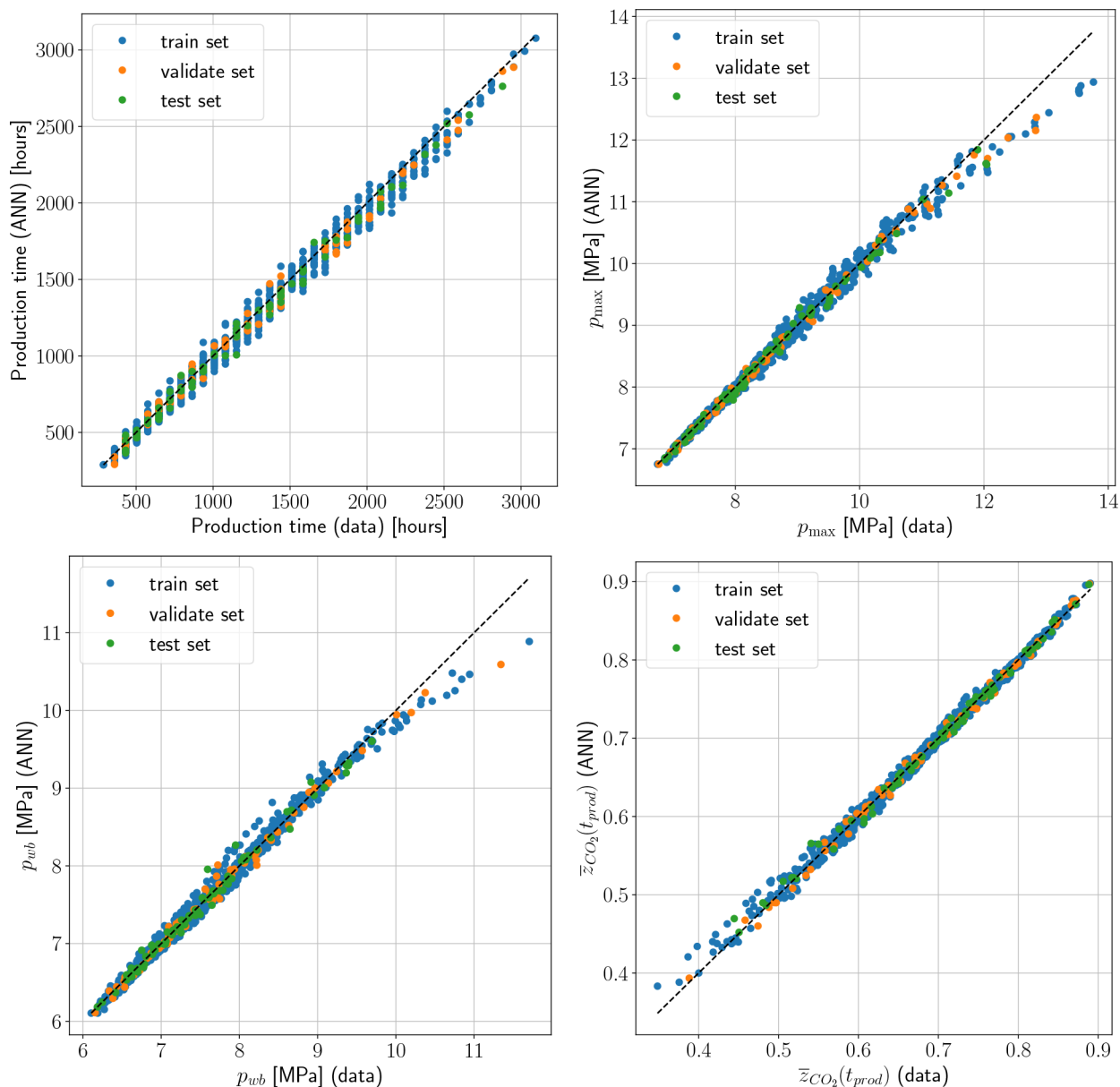


Figure 12. Performance of the ANN model for case 10 with respect to the four output parameters t_{prod} (top, left), p_{\max} (top, right), p_{wb} (bottom, left), and \bar{z}_{CO_2} (bottom, right), using 87.5% of the data in the training and 6.25% each for validation and testing.

norm during the training of the ANN model for case 5. The results show that the performance deteriorates when using weights of 10^{-3} . In this case, the loss function and mean squared error both reside at a higher level at the end of training, and the resulting RMSE and R^2 score are 0.03 and 0.98, respectively.

3.2. ANN Models with Multiple Output Parameters.

The inclusion of the derived parameters did not significantly impact the predictive performance of the two ANN models for p_{\max} and t_{prod} . Here, we use the architecture of the ANN model for t_{prod} (case 3) and explore its performance when augmenting the output layer to enable simultaneous prediction of multiple parameters that are important to UNGS with cushion CO_2 . With reference to Table 3, we extend the output as described in case 6 to case 10 and train the models again. The number of input parameters remains fixed. Note that we do not explore the use of $\bar{z}_{CO_2}(t_{inj})$ and $\bar{p}(t_{prod})$ in these ANNs, as their behaviors are very

similar to $\bar{z}_{CO_2}(t_{prod})$ and $p_{wb}(t_{prod})$, respectively, as discussed in section 2.3 (cf. Figure 6).

Following Ali,¹⁸ we also explore the performance of the resulting ANNs when reducing the amount of data used in the training. For this purpose, we train the networks for cases 6–10 on three extracted data sets obtained with $N_v = 75, 150,$ and 300 , respectively. Thus, the corresponding training data sets constitute results from 1050 (87.5%), 900 (75%), and 600 (50%) simulations. If each of the five input parameters was varied an equal number of times in the MRST simulations, this corresponds to the scenario where each parameter on average is varied $4.02 (= 1050^{1/5})$, $3.90 (= 900^{1/5})$, and $3.59 (= 600^{1/5})$ numbers of times in these differently sized training data sets. The remaining data is split in two equal parts, used for validation and testing.

Cases 6–8 investigate the ANN capability with the inclusion of either p_{\max} (case 6), the well-block pressure $p_{wb}(t_{prod})$ (case 7), or average mole fraction in the reservoir, $\bar{z}_{CO_2}(t_{prod})$ (case 8), as

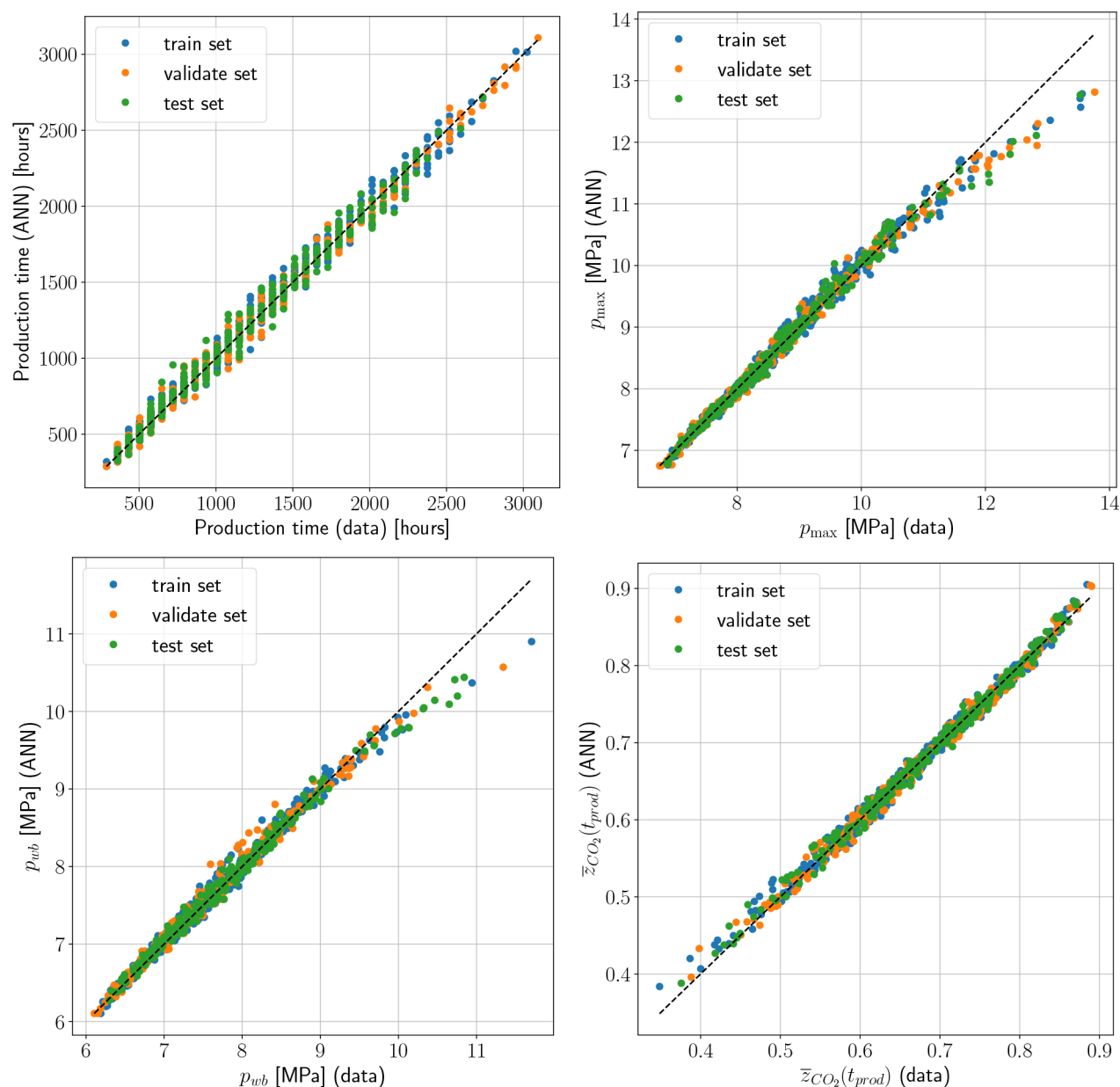


Figure 13. Performance of the ANN model for case 10 with respect to the four output parameters t_{prod} (top, left), p_{\max} (top, right), p_{wb} (bottom, left), and \bar{z}_{CO_2} (bottom, right), using 50% of the data in the training and 25% each for validation and testing.

an additional output parameter alongside t_{prod} in the ANN model. Table 5 presents estimates for the overall RMSE and R^2 scores based on all the output data (nondimensionalized and rescaled to the interval [0,1]) in these ANN models using 87.5% of the data for training. Compared with the excellent results for t_{prod} in case 3 (with RMSE around 0.011 and R^2 score of 0.9975, cf. Table 4), the addition of another parameter in the ANN model degrades the performance slightly, with RMSEs between 0.012 and 0.017 and R^2 scores from 0.993 to 0.996. With respect to these metrics, case 8 performs best, suggesting $\bar{z}_{CO_2}(t_{prod})$ is less challenging to predict accurately with ANN models than the pressures p_{\max} and $p_{wb}(t_{prod})$.

Tables 6 and 7 present the performance of the corresponding ANNs using 75% and 50% of the data for training, respectively. Reducing the amount of training data reduces the accuracy of the ANN for case 8, while case 6 and case 7 remain largely unaffected. With a share of 75% training data, the overall RMSEs

are between 0.013 and 0.016 and the overall R^2 scores are between 0.994 and 0.996, while for a share of 50% the RMSEs are between 0.014 and 0.017 and the R^2 scores range from 0.991 to 0.995. Figure 10 supports these findings as the ANN predictions against data for case 6 with shares of 87.5% and 50% of the data in the training are very similar. However, in comparison with the single-output ANNs (cases 1 and 3 shown in Figures 7 and 8, respectively), there is a larger discrepancy in the predictions of both p_{\max} and t_{prod} . In case 6, the disparity at high p_{\max} is more visible than in the single-output ANN models (cf. Figure 7).

The ANN model for case 9 takes the three parameters t_{prod} , p_{\max} , and $p_{wb}(t_{prod})$ as output. Figure 11 shows the ANN calculations of all output parameters versus the simulated data. A reduction in the share of training data from 87.5% to 50% does not impact the model performance significantly. Both models exhibit an increased deviation from the data for high p_{\max} and p_{wb}

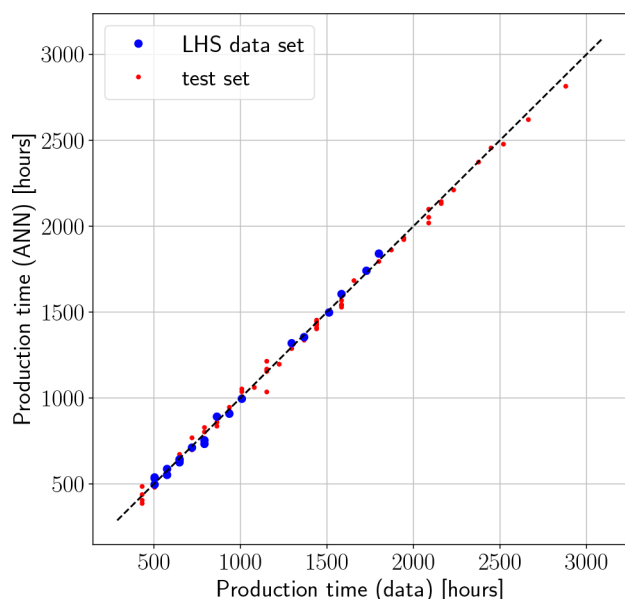


Figure 14. Predictions of t_{prod} using the ANN model for case 3 on sampled data (LHS data set) compared to corresponding MRST simulation results. The ANN model was trained on 87.5% of the original MRST simulations with systematic variation of input parameters. For comparison with the LHS data set, the figure also shows the results from the test set which constitute 6.25% of the previously generated data.

where data is scarce. Looking at Figure 6, the Pearson correlation between p_{max} and p_{wb} is 0.79, which indicates that in many scenarios, high p_{max} and p_{wb} describe similar conditions where the ANN models are less accurate. However, this is not always the situation; the horizontal permeability K_{h} represents an exception to this behavior as its Pearson correlations with p_{max} and p_{wb} are -0.06 and 0.45 , respectively. Figure 4 (fourth row) supports this behavior further; lower K_{h} leads to higher p_{max} and lower p_{wb} . Tables 5–7 show that case 9 yields RMSE estimates between 0.014 and 0.017 and R^2 scores between 0.992 and 0.995. Hence, an extension of the number of output parameters from two to three did not lead to any noteworthy losses of accuracy in the ANN predictions.

Finally, the ANN model of case 10 augments the output layer to enable simultaneous predictions of t_{prod} , p_{max} , $p_{\text{wb}}(t_{\text{prod}})$, and $\bar{z}_{\text{CO}_2}(t_{\text{prod}})$. Figures 12 and 13 show ANN calculations of all four output parameters compared with the generated data when the share of training data is 87.5% and 50%, respectively. Overall, the ANN calculations of t_{prod} display a larger spread in a thicker band around the ideal line in the plot, whereas the results for high values of p_{max} and p_{wb} deviate more than in the previous cases. The ANN model shows the best performance for the average mole fraction, \bar{z}_{CO_2} , except for a deviation at low values. From Figure 6, the Pearson correlation coefficients between \bar{z}_{CO_2} and the pressures p_{max} and p_{wb} are -0.78 and -0.93 , respectively, which overall suggests that a low \bar{z}_{CO_2} corresponds to high p_{wb} and often a high p_{max} . In terms of the performance metrics, Tables 5–7 show that the ANN model with an 87.5% share of training data performs slightly better than the model with only a 50% share of training data. The overall RSMs range from 0.016 to 0.019, while the R^2 scores range from 0.989 to 0.992.

3.3. Application of the ANN Models on Sampled Data. Thus far, we have demonstrated the accuracy of the developed

ANN models by only using data from reservoir simulations generated with systematic variation of the input parameters (H , T , ϕ , K_{h} , t_{inj}). Here, we explore the predictive capabilities of the ANN models on 20 new data sets where the values of the input parameters are generated with Latin hypercube sampling (LHS).³¹ The sampling method uses the maximum and minimum values of each parameter in Table 1 as the upper and lower limits in the parameter generation. The sampled data provide input to the ANN models as well as 20 new MRST simulations with otherwise the same specifications as those described in section 2.3. The data from these MRST simulations were saved in a separate .xlsx file (available in Supporting Information) and used for comparisons against the predictions of the output parameters from the ANN models for case 3 and case 10. Figure 14 presents this comparison for the ANN model of case 3, which was trained with data from 1050 (87.5%) of the original MRST simulations. The ANN predictions exhibit excellent results, with an RMSE of 0.009 and an R^2 score of 0.996. Figure 15 shows that the ANN model for case 10, trained with data from 600 (50%) of the original simulations, accurately describes the output parameters t_{prod} , p_{max} , $p_{\text{wb}}(t_{\text{prod}})$, and $\bar{z}_{\text{CO}_2}(t_{\text{prod}})$ from the new MRST simulations with sampled input data. We performed the same exercise using the ANN model for case 10 trained on 1050 (87.5%) of the original data sets. In both cases, the estimates of RMSE and R^2 are 0.010 and 0.991, respectively.

The results also show that a small number of 20 sampled data is insufficient to assess the behavior at high values of t_{prod} , which typically corresponds to data combinations with long injection times t_{inj} , as well as low K_{h} and H . Similarly, an evaluation of ANN predictions in the range with high p_{max} and p_{wb} requires that the sampling method provides data combinations with high t_{inj} and low ϕ and H . This also points at an abundance of training data at low and intermediate values of p_{max} and p_{wb} , which likely leads to a lower accuracy of the ANN models at high values of pressure where the amount of data from the original MRST simulations is scarcer (cf. Figure 13).

3.4. Discussion. The ANN models proposed in this work are useful tools that could both aid in the selection of the most suitable site for gas storage with cushioned CO_2 as well as provide guidance in the initial planning of a seasonal gas storage cycle. Training of such ANN models on data from 3D reservoir simulations will provide fast identification of optimal parameter combinations for a prolonged withdrawal time of CH_4 with minimal CO_2 production from the top zone of the reservoir where only a small or negligible amount of water resides. These initial ANN calculations guide the selection of input parameters for more detailed reservoir simulations of the most promising scenarios that is possible for the facility as identified by the ANN models. The focus here has been on determining the time t_{prod} at which the well-block mole fraction exceeds 1% CO_2 . The favorable results suggest it is also possible to develop ANN models for the full relationship between well-block mole fraction and production time or rather specify the production time as input and predict the well-block mole fraction. Simultaneously, the ANN models provide information on constraining factors for the operation of the gas storage facility, such as the maximal pressure which should not become too high to avoid damaging the rock and change its permeability in an unpredictable manner.⁹

There is enormous potential for saving time by performing calculations with ANN models instead of reservoir simulators.

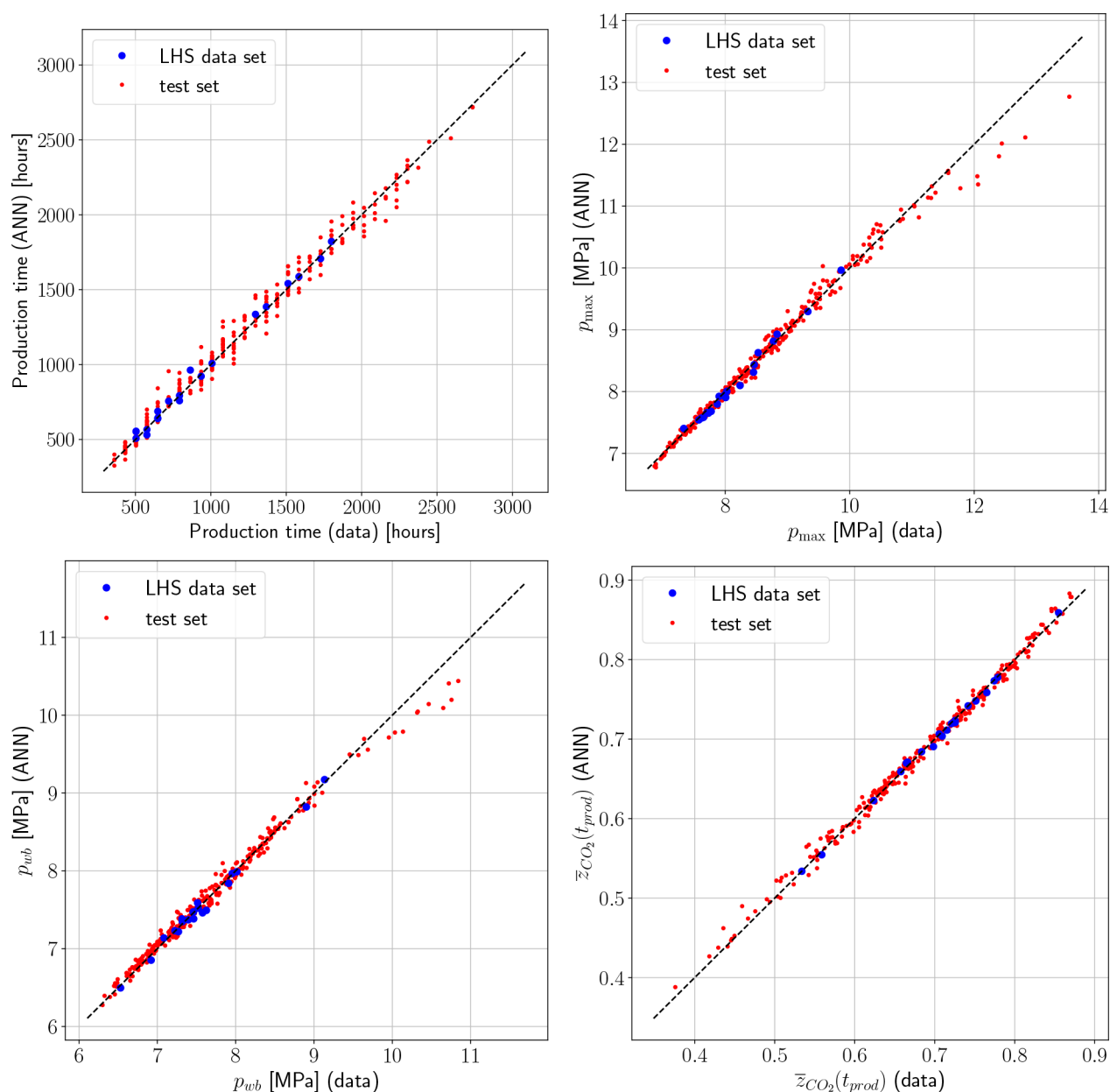


Figure 15. Predictions with the ANN model for case 10 on sampled data (LHS data set) compared with the results from new MRST simulations with respect to the four output parameters t_{prod} (top, left), p_{max} (top, right), p_{wb} (bottom, left), and \bar{z}_{CO_2} (bottom, right). The ANN model was trained on 50% of the original MRST simulations with a systematic variation of input parameters. For comparison with the LHS data set, the figures also show the results from the test set, which constitutes 25% of the previously generated data.

For the MRST simulation with midrange parameters in section 2.3, the wall-clock time of the simulation is 234.8 s, using a Lenovo X390 Yoga laptop with a Windows 10 Pro operating system, Intel Core i7–8565U CPU @ 18.0 GHz, and 16.0 GB of RAM. Changing H to its minimum value, which corresponds to the smallest number of grid blocks, reduces the simulation time to 123.3 s, while changing H to its maximum value yields the largest number of grid blocks and a simulation time of 413.0 s. In comparison, data processing and training the ANN models for case 10 on 87.5% and 50% of the data, followed by making the predictions, generates wall-clock times of respectively 26.1 and 22.2 s in total, using the same laptop. However, the potential for saving time by using ANN models is much larger, in comparison against 3D reservoir simulations.

Overall, the results presented in this work suggest that, with five varied input parameters, the training of the ANN models could be performed with a smaller amount of data generated from the simulations. In this work, a systematic and independent variation of the five parameters shows that a reduction in the amount of training data from 1050 to 600 equiv introduces only a minor loss of accuracy in the ANN predictions.³¹ Future work will explore if advanced sampling strategies³¹ can guide the generation of a sufficient amount of data for UNGS with CO₂ cushion gas. This is important in extensions of the idealized reservoir setup explored here, which likely will require the variation of additional parameters in simulations. As examples, reservoirs with nonzero inclination angles have been shown to be advantageous for UNGS,⁹ while a surface roughness of the caprock likely will impact the lateral transport of CH₄ as

previously investigated for CO₂ migration.³² Further, the presence of a water phase^{5,7} introduces convective mixing,³³ wetting behavior, capillary trapping, and related diffusion.^{6,34} On the other hand, some parameters could assume a correlation, as is often the case with permeability and porosity, depending on rock type.³⁵ In this work, we varied these two parameters independently, and hence, the simulation results likely capture any such correlations. Last, there is also room to vary other parameters that we have treated as constants here, including the initial reservoir pressure and injection/production rate. This renders possible investigations of the relation between well-block pressure, reservoir pressure, and gas deliverability.¹⁵

4. CONCLUSIONS

This work applied compositional reservoir simulations on an idealized reservoir with one well to investigate a seasonal cycle of CH₄ injection and production, using CO₂ as cushion gas. For this purpose, we used the open-source simulator MRST, which was shown to yield consistent results with the commercial simulator CMG-GEM for the reservoir setup considered here. Then, MRST simulations with independent variations of five input parameters (reservoir temperature, height, porosity, permeability, and injection time) generated data from 1200 cases that captured various conditions. The results show that the reservoir height and permeability are the most influential parameters for the well-block mole fraction during production.

The generated data were used to develop two ANN models that describe separately the maximum reservoir pressure and the production time until the CO₂ mole fraction in the well block exceeds 1%, using the five varied parameters from the simulations as input. These ANN models exhibit excellent performance, and the inclusion of volume of cushion gas as a derived input parameter to the ANNs did not improve the results any further.

The network structure of the ANN model for production time was trained again after augmenting its output with up to three more parameters: the maximum pressure as well as the well-block pressure and average reservoir mole fraction at the end of production. We also investigated the impact of reducing the data share used in the training from 87.5% to 50%. Overall, an increase in the amount of output parameters leads to a slightly reduced accuracy in the ANN predictions for all of the output parameters, especially at conditions with high maximum reservoir pressure and high well-block pressure. On the other hand, a reduction in the amount of training data had almost negligible impact on the predictive capabilities of the ANN models. In all cases, the developed ANN models perform well with an RMSE lower than 0.02 and an R² score above 0.99. Testing of the ANN models on a new set of data generated with Latin hypercube sampling showed excellent agreement with the corresponding reservoir simulations. Hence, we conclude that trained and validated ANNs are capable tools for describing relations between important parameters in UNGS operations that utilize CO₂ as cushion gas, with the aim of reaching higher CH₄ production time, larger amounts of delivered gas, and minimal CO₂ production.

A natural extension of this work is to explore the use of data-driven methods to describe production behavior over multiple cycles of seasonal CH₄ storage with different schedules for injection and production and to optimize the placements of cushion CO₂ injection wells and CH₄ injection and production wells.

■ ASSOCIATED CONTENT

Supporting Information

The Supporting Information is available free of charge at <https://pubs.acs.org/doi/10.1021/acs.energyfuels.3c03382>.

Data saved from the 1200 MRST simulations with the different parameters organized column-wise and the data from the simulations organized row-wise (one row of data per simulation); first row specifies the parameters and their units (XLSX)

Data saved from 20 MRST simulations where the varied input data (H , T , ϕ , K_{lv} , t_{inj}) are generated with Latin hypercube sampling, with the different parameters organized column-wise and the data from the simulations organized row-wise (one row of data per simulation); first row specifies the parameters and their units (XLSX)

■ AUTHOR INFORMATION

Corresponding Author

Johan Olav Helland – Department of Energy and Petroleum Engineering, University of Stavanger, N-4036 Stavanger, Norway; orcid.org/0000-0002-4330-101X; Email: johan.o.helland@uis.no

Authors

Helmer André Friis – Department of Energy and Petroleum Engineering, University of Stavanger, N-4036 Stavanger, Norway; orcid.org/0000-0003-2462-1381

Mohsen Assadi – Department of Energy and Petroleum Engineering, University of Stavanger, N-4036 Stavanger, Norway

Łukasz Klimkowski – AGH University of Kraków, 30-059 Kraków, Poland

Stanisław Nagy – AGH University of Kraków, 30-059 Kraków, Poland

Complete contact information is available at:

<https://pubs.acs.org/doi/10.1021/acs.energyfuels.3c03382>

Notes

The authors declare no competing financial interest.

■ ACKNOWLEDGMENTS

This research was funded by EEA and Norway Grants, operated by The National Center for Research and Development, grant number NOR/POLNORCCS/AGaStor/0008/2019-00.

■ REFERENCES

- (1) International Energy Agency (IEA). Energy Technology Perspectives 2023. Available online, 2023: <https://www.iea.org/reports/energy-technology-perspectives-2023>.
- (2) International Energy Agency (IEA). Fuel & technologies, Gas. Available online: <https://www.iea.org/fuels-and-technologies/gas>.
- (3) U.S. Energy Information Administration (EIA). The Basics of Underground Natural Gas Storage. Natural gas report. November 16, 2015. Available online: <https://www.eia.gov/naturalgas/storage/basics/>.
- (4) Wang, X.; Economides, M. *Advanced Natural Gas Engineering*; Elsevier Science, 2013.
- (5) Oldenburg, C. M. Carbon dioxide as cushion gas for natural gas storage. *Energy Fuels* **2003**, *17*, 240–246.
- (6) Special Issue commemorating the 10th year anniversary of the publication of the Intergovernmental Panel on Climate Change Special Report on CO₂ Capture and Storage: Krevor, S.; Blunt, M. J.; Benson, S. M.; Pentland, C. H.; Reynolds, C.; Al-Menhali, A.; Niu, B. Capillary

trapping for geologic carbon dioxide storage – From pore scale physics to field scale implications. *International Journal of Greenhouse Gas Control* **2015**, *40*, 221–237.

(7) Cao, C.; Liao, J.; Hou, Z.; Xu, H.; Mehmood, F.; Wu, X. Utilization of CO₂ as Cushion Gas for Depleted Gas Reservoir Transformed Gas Storage Reservoir. *Energies* **2020**, *13*, 576.

(8) Flanigan, O. *Underground Gas Storage Facilities*; Gulf Professional Publishing, 1995.

(9) Ma, J.; Li, Q.; Kempka, T.; Kühn, M. Hydromechanical response and impact of gas mixing behavior in subsurface CH₄ storage with CO₂-based cushion gas. *Energy Fuels* **2019**, *33*, 6527–6541.

(10) Sadeghi, S.; Sadaee, B. Mechanistic simulation of cushion gas and working gas mixing during underground natural gas storage. *Journal of Energy Storage* **2022**, *46*, 103885.

(11) Song, Y.; Sung, W.; Jang, Y.; Jung, W. Application of an artificial neural network in predicting the effectiveness of trapping mechanisms on CO₂ sequestration in saline aquifers. *International Journal of Greenhouse Gas Control* **2020**, *98*, 103042.

(12) Wen, G.; Li, Z.; Azizzadenesheli, K.; Anandkumar, A.; Benson, S. M. U-FNO—An enhanced Fourier neural operator-based deep-learning model for multiphase flow. *Advances in Water Resources* **2022**, *163*, 104180.

(13) Chu, A. K.; Benson, S. M.; Wen, G. Deep-learning-based flow prediction for CO₂ storage in shale-sandstone formations. *Energies* **2023**, *16*, 246.

(14) Van, S. L.; Chon, B. H. Effective Prediction and Management of a CO₂ Flooding Process for Enhancing Oil Recovery Using Artificial Neural Networks. *J. Energy Resour. Technol.* **2018**, *140*, 032906.

(15) Ali, A. Data-driven based machine learning models for predicting the deliverability of underground natural gas storage in salt caverns. *Energy* **2021**, *229*, 120648.

(16) Vo Thanh, H.; Zamanyad, A.; Safaei-Farouji, M.; Ashraf, U.; Hemeng, Z. Application of hybrid artificial intelligent models to predict deliverability of underground natural gas storage sites. *Renewable Energy* **2022**, *200*, 169–184.

(17) Mann, A. W., III; Ayala, L. F. Intelligent design and modelling of natural gas storage facilities. *Int. J. Modelling and Simulation* **2009**, *29*, 214–223.

(18) Lie, K. A. *An Introduction to Reservoir Simulation Using MATLAB/GNU Octave: User Guide to the MATLAB Reservoir Simulation Toolbox*; Cambridge University Press, 2019.

(19) Lie, K. A.; Møyner, O. *Advanced Modeling with the MATLAB Reservoir Simulation Toolbox*; Cambridge University Press, 2021; Chapter 8, pp 324–374.

(20) *ECLIPSE Reservoir Simulation Software: Technical Description*, 2014.1 edition; Schlumberger, 2014.

(21) Voskov, D. V.; Tchelepi, H. A. Comparison of nonlinear formulations for two-phase multi-component EoS based simulation. *J. Pet. Sci. Eng.* **2012**, *82–83*, 101–111.

(22) *CMG GEM User's Guide*; Computer Modeling Group Ltd.: Calgary, Alberta, Canada, 2015.

(23) Ahmed, T. In *Reservoir Engineering Handbook*, fifth ed.; Ahmed, T., Ed.; Gulf Professional Publishing, 2019; pp 1109–1225.

(24) Lohrenz, J.; Bray, B. G.; Clark, C. R. Calculating viscosities of reservoir fluids from their compositions. *Journal of Petroleum Technology* **1964**, *16*, 1171–1176.

(25) Fanchi, J. R. In *Integrated Reservoir Asset Management*; Fanchi, J. R., Ed.; Gulf Professional Publishing: Boston, 2010; pp 49–69.

(26) Goupil, M.; Heap, M. J.; Baud, P. Permeability anisotropy in sandstones from the Soultz-sous-Forêts geothermal reservoir (France): implications for large-scale fluid flow modelling. *Geotherm Energy* **2022**, *10*, 32.

(27) Shikhov, I.; d'Eurydice, M. N.; Arns, J.; Arns, C. H. An experimental and numerical study of relative permeability estimates using spatially resolved T₁ – z NMR. *Transport in Porous Media* **2017**, *118*, 225–250.

(28) Shah, S.; Gray, F.; Crawshaw, J.; Boek, E. Micro-computed tomography pore-scale study of flow in porous media: Effect of voxel resolution. *Advances in Water Resources* **2016**, *95*, 276–287.

(29) Bjørkum, P. A.; Nadeau, P. H. Temperature controlled porosity/permeability reduction, fluid migration, and petroleum exploration in sedimentary basins. *APPEA Journal* **1998**, *38*, 453–465.

(30) Kingma, D. P.; Ba, J. Adam: A method for stochastic optimization. *arXiv preprint* **2014**, arXiv:1412.6980.

(31) Shields, M. D.; Zhang, J. The generalization of Latin hypercube sampling. *Reliability Engineering & System Safety* **2016**, *148*, 96–108.

(32) Gasda, S. E.; Nilsen, H. M.; Dahle, H. K.; Gray, W. G. Effective models for CO₂ migration in geological systems with varying topography. *Water Resour. Res.* **2012**, *48*, W10546.

(33) Jiang, L.; Wang, Y.; Lu, G.; Yang, J.; Song, Y. Experimental Study on the Density-Driven Convective Mixing of CO₂ and Brine at Reservoir Temperature and Pressure Conditions. *Energy Fuels* **2022**, *36*, 10261–10268.

(34) Singh, D.; Friis, H. A.; Jettestuen, E.; Helland, J. O. Pore-scale Ostwald ripening of gas bubbles in the presence of oil and water in porous media. *J. Colloid Interface Sci.* **2023**, *647*, 331–343.

(35) Pape, H.; Clauser, C.; Iffland, J. Chapter: Variation of Permeability with Porosity in Sandstone Diagenesis Interpreted with a Fractal Pore Space Model. In *Fractals and Dynamic Systems in Geoscience*; Blenkinsop, T. G., Kruhl, J. H., Kupková, M., Eds.; Birkhäuser Basel: Basel, 2000; pp 603–619.